Aalborg Universitet

AALBORG UNIVERSITY
DENMARK

Adaptive Grid Impedance Shaping Approach Applied for Grid-Forming Power Converters

De Araujo Ribeiro, Ricardo Lucio; Oshnoei, Arman; Anvari-Moghaddam, Amjad; Blaabjerg, Frede

Published in:
IEEE Access

DOI (link to publication from Publisher):
10.1109/ACCESS.2022.3196921

Creative Commons License
CC BY 4.0

Publication date:
2022

Document Version
Publisher's PDF, also known as Version of record

Link to publication from Aalborg University

Citation for published version (APA):
De Araujo Ribeiro, R. L., Oshnoei, A., Anvari-Moghaddam, A., & Blaabjerg, F. (2022). Adaptive Grid Impedance Shaping Approach Applied for Grid-Forming Power Converters. *IEEE Access*, *10*, 83096-83110. https://doi.org/10.1109/ACCESS.2022.3196921

General rights
Copyright and moral rights for the publications made accessible in the public portal are retained by the authors and/or other copyright owners and it is a condition of accessing publications that users recognise and abide by the legal requirements associated with these rights.

- Users may download and print one copy of any publication from the public portal for the purpose of private study or research.
- You may not further distribute the material or use it for any profit-making activity or commercial gain
- You may freely distribute the URL identifying the publication in the public portal -

Take down policy
If you believe that this document breaches copyright please contact us at vbn@aub.aau.dk providing details, and we will remove access to the work immediately and investigate your claim.

IEEE Access
Multidisciplinary | Rapid Review | Open Access Journal

Received 6 June 2022, accepted 27 July 2022, date of publication 5 August 2022, date of current version 11 August 2022.

Digital Object Identifier 10.1109/ACCESS.2022.3196921

RESEARCH ARTICLE

Adaptive Grid Impedance Shaping Approach Applied for Grid-Forming Power Converters

RICARDO LUCIO DE ARAUJO RIBEIRO[1], (Senior Member, IEEE), ARMAN OSHNOEI[2], (Member, IEEE), AMJAD ANVARI-MOGHADDAM[2], (Senior Member, IEEE), AND FREDE BLAABJERG[2], (Fellow, IEEE)

[1]Department of Electrical Engineering, Federal University of Rio Grande do Norte (UFRN), Natal 59072-970, Brazil
[2]AAU Energy, Aalborg University, 9220 Aalborg, Denmark

Corresponding author: Ricardo Lucio de Araujo Ribeiro (rlucio@dee.ufrn.br)

The work of Ricardo Lucio de Araujo Ribeiro was supported by the Brazilian National Science Foundation CAPES.

ABSTRACT This paper proposes an adaptive grid impedance shaping approach, implemented through a variable structure virtual impedance control strategy (VS-VIS), to improve the power flow control of grid-forming power converters (GF-PC). In this strategy, an equivalent grid impedance estimator (EGIE) evaluates the feeder X/R ratio to determine the required virtual impedance to reach the grid shaping objective. Besides, the virtual impedance definition also considers the converter power rating to ensure the system's feasibility. A virtual negative resistance series interconnected with a positive virtual reactance implements the virtual impedance. Moreover, the required virtual impedance is only updated when the X/R ratio extrapolates deviation limits determined by allowed grid voltages boundaries specified by the standards. Besides, the virtual reactance is split into two parts that use the conventional and sliding mode (SMC) approaches. The first implements the main part of required virtual reactance, while the second provides a fine-tuning action matching the X/R control objectives and compensating grid impedance uncertainties. This grid-shaping method provides a smooth compensation increasing the GF-PC resilience under grid impedance variation. These features constitute a novelty compared to the shaping methods presented in the literature. Experimental tests obtained from a GF-PC laboratory setup demonstrate the effectiveness and robustness of the proposed grid impedance shaping method.

INDEX TERMS Virtual impedance, variable control structure, power decoupling, grid impedance estimation.

I. INTRODUCTION

The distributed generators (DGs) are interconnected to microgrids (MG) through active front-end converters, controlled to provide the required power-sharing under grid-connected or islanded operation modes. These converters operate as grid-forming power converters (GF-PC), providing voltage and frequency support to the networks. On the other hand, those inverters are controlled as voltage sources, parallel connected to the MG in islanded conditions. Both conditions demand active and reactive powers to afford suitable power-sharing and guarantee the required MG stability [1]. Ideally, each DG must operate independently without communication for practical and economic aspects.

The most common control strategy employed to fulfill the proper power flow regulation uses droop control approaches, mimicking the behavior of standard synchronous generators [1], [2]. Those control approaches require a feeder with an inductive profile, directly correlating the active power with the system frequency and reactive power with the system voltage. However, these conditions refer to medium or high voltage microgrids (i.e., high X/R ratio) [3]. On the other hand, low voltage microgrids depict line impedance with small X/R ratios, resulting in active and reactive power coupling conditions, which deteriorates the system's dynamic response and stability [4]. In this case, modified droop control methods associated with power decoupling approaches have

The associate editor coordinating the review of this manuscript and approving it for publication was Jiefeng Hu.

This work is licensed under a Creative Commons Attribution 4.0 License. For more information, see https://creativecommons.org/licenses/by/4.0/

been proposed to improve the power-sharing accuracy of those networks [5].

Generally, the power decoupling approaches can be divided into two categories [6]: open-loop [6]–[12] or closed-loop [11], [13]–[18] power decoupling strategies (i.e., OL-PDS or CL-PDS, respectively). OL-PDS schemes are more straightforward to implement than the CL-PDS approaches and can be divided into virtual impedance decoupling strategies (VI-DS) [7]–[9], [11] and Q-V modified droop control (QV-MDC) [6], [10], [11]. The VI-DS incorporates a virtual impedance by inserting a feed-forward control scheme to reshape the DG output impedance to depict inductive or resistive characteristics, allowing it to independently control active and reactive powers. In this direction, the implementation of a virtual impedance composed of the series connection of negative resistance and inductance reshapes the equivalent impedance between a virtual power source (VPS) and the point of common coupling (PCC) [11], making it being inductive and permitting a suitable power-sharing. In general, VI-DS methods are based on the explicit recognition of the microgrid structure to provide accurate power-sharing, which is no longer valid when those structural changes [9], [19]. It is possible to mitigate these inaccuracies by estimating the DG equivalent impedance using the DG output currents, voltages, and feeder nameplate impedance, as proposed in [8]. However, it still has uncertainties due to possible parameter variations, which could be circumvented using an adaptive virtual impedance [8]. Consensus-based controllers could also adjust the virtual impedance adaptively, overcoming possible mismatches provoked by grid impedance variation [20]–[22]. However, this methodology utilizes many control loops, increasing the complexity of implementation and producing large values of the virtual impedance, resulting in undesired power quality issues.

Unlike the VI-DS methods, the QV-MDC approach improves the reactive power-sharing accuracy by using a voltage restoration mechanism without modifying the DG output impedance [6]. The main drawback of this control approach is the necessity of defining different set-points based on the DG characteristics, which could make the QV-MDC ineffective [10]. Therefore, a modified voltage restoration based on local information was proposed in [12] to overcome the set-point deviation. Nevertheless, despite QV-MDC being effective under an inductive profile, its performance degrades when the feeder equivalent impedance is complex. In this sense, a virtual complex impedance based on the P-V droop method applied for low-voltage microgrid power-sharing, composed of a VI-DS and QV-MDC association, was proposed in [23]. This methodology employed an extra parameter to accelerate the dynamic regulation and active power-sharing.

The CL-PDS can be classified as follows: small-signal injection [13]–[16], PCC voltage detection [11], [18], load changing detection [15], impedance droop estimation [17], or virtual power source [11], [18]. The small-signal injection methods [16] employ an ac low-voltage signal added to the voltage reference to provoke a controlled disturbance at the PCC. This procedure can extract the required grid information but depicts a relatively complex implementation. PCC voltage detection approaches [13], [14] are unsuitable for practical applications since most DGs are installed dispersedly. The load change detection scheme can be implemented through signal processing approaches like wavelet transform as proposed in [15], [24], but its use in closed-loop control schemes is inappropriate. The impedance droop estimation permits the local loads compensation, providing suitable power-sharing in grid-connected and islanded modes [17]. However, its accuracy depends on the system operating condition, which can be essential. The virtual power source control scheme decouples the active and reactive powers by rotating the reference frame by the impedance phase angle [11]. However, this method fails in sharing the actual power when the distribution line impedance of each DG is different. This drawback could be mitigated if the rotation is implemented through an optimal angle obtained from system stability analysis [18]. Nevertheless, non-identical frequency in the DGs power converters could occur, resulting in asynchronous controller operation, leading to instability issues.

Most of the grid-shaping methods presented in the literature depend on the knowledge of grid impedance parameters, making them ineffective under uncertainties caused by grid impedance variations. They generally employ compensation mechanisms that provide grid-shaping actions inside an expected grid parameters range. Besides, they use virtual reactive components to achieve the X/R control objective, and their implementation can cause voltage oscillations under abrupt grid impedance variations.

This paper proposes an adaptive grid shaping approach, implemented through a variable structure virtual impedance strategy (VS-VIS), to improve the power flow regulation of GF-PC under uncertainties caused by grid impedance variations. In this method, an equivalent grid impedance estimator (EGIE) evaluates the feeder X/R ratio to determine the required virtual impedance profile and components to reach the grid shaping objective. Besides, the chosen virtual impedance also considers the converter power rating to ensure the system's feasibility. This work employs a series association of virtual negative resistance with a positive virtual reactance, in which their values consider the network damping condition and the required X/R control objective. Unlike the implementation of virtual resistance, the insertion of reactive elements causes oscillations in the GF-PC terminal voltages. Because of this, the proposed methodology employs an updating scheme to define the value of reactance that will be implemented. Thus, despite the continuous EGIE estimation, the value of virtual reactance that will be employed is only updated when X/R extrapolates deviations thresholds imposed by the allowed power grid voltage boundaries specified by the standards. This procedure introduces an X/R dead zone, where grid impedance variation occurrences do not update the value of virtual reactance. For that reason, the

implementation of the required virtual reactance is split into two parts that use both a conventional and a sliding mode (SMC) [25] approaches. The first is responsible for compensating most of the required virtual reactance, and the second provides a fine-tuning action matching the control objectives and compensating uncertainties inside the X/R dead-zone. This grid-shaping approach provides a smooth compensation increasing the GF-PC resilience under grid impedance variation. These features comprise a novelty compared to the grid-shaping methods presented in the literature. Experimental tests are obtained from a GF-PC laboratory setup, operating under different operational conditions, demonstrating the effectiveness and robustness of the proposed grid shaping method.

The rest of this paper is organized as follows. First, section II describes the proposed system, modeling, and control strategies employed in the proposed GF-PC. Next, section III deals with the adaptive grid impedance shaping approach, based on variable structure virtual impedance strategy and the system stability analysis. Then, in section IV, experimental results obtained from a GF-PC functioning under different operational scenarios demonstrate de feasibility of the proposed method. Finally, Section V the conclusions on the contributions of the paper.

II. SYSTEM DESCRIPTION, MODELING AND CONTROL

Fig. 1 depicts the configuration of the laboratory setup employed to evaluate the proposed adaptive grid shaping strategy. It comprises a GF-PC, interconnected to the PCC through a line transmission emulated by a three-phase RL branch ($z_s = r_s + j\omega l_s$). In addition, a three-phase RL load ($z_l = r_l + j\omega l_l$), with configurable parameters, is also interconnected to the PCC to evaluate the system's performance with load change. Furthermore, the controlled switch S_{w1} connects a three-phase resistive load (r_{lext}) with the RL load, which can provoke a controlled load change. Also, external resistors (r_{ext}) are used to modify the grid impedance parameters through the controlled switch S_{w2}. Besides, a power grid emulator (PGE) commanded by a digital real-time simulator (DRTS) implements the power grid. The implementation of the GF-PC comprises a voltage source converter interconnected to the PCC through an LC filter, controlled by the voltage regulator and synchronous power controller, according to Fig. 1. In addition, the proposed adaptive grid impedance shaping approach comprises an equivalent grid impedance estimator, decision logic system, and variable structure virtual impedance system, represented by blocks EGIE, DLS, and VS-VIS in Fig. 1. Finally, a dSPACE fast prototyping system executes both algorithms of the GF-PC control system and the adaptive grid shaping approach. The modeling and control approaches used in the proposed method are detailed below.

A. VOLTAGE CONTROL STRATEGY

The voltage control strategy employs a cascaded regulator approach in which the inner loop controls the LC filter input current, and the outer loop controls the GF-PC output voltage (i.e., blocks $R_i(s)$ and $R_v(s)$ in Fig. 1). In this approach, the inner loop employs a simple proportional controller (P), while a proportional-resonant regulator (PR), tuned at the fundamental frequency, implements the outer loop [26].

The implementation and design of the voltage regulator follow the pole placements and tracking objectives as proposed in [27], which can be described by the following control laws

$$Q_m(s)L(s)i^*_{g\alpha\beta}(s) = -P(s)(v^*_{g\alpha\beta}(s) - v_{g\alpha\beta}(s)), \tag{1}$$

where $Q_m(s)$ is the internal model of reference voltages $v^*_{g\alpha\beta}(s)$, $P(s)$ and $L(s)$ are polynomials, with $L(s)$ being monic. The choice of $Q_m(s)$ must satisfy $Q_m(s)v^*_{g\alpha\beta}(s) = 0$, resulting in the following controller transfer function

$$R_v(s) = \frac{P(s)}{Q_m(s)L(s)}. \tag{2}$$

The voltage-current transfer function of the LC filter on the stationary reference frame can be described as

$$v_{g\alpha\beta}(s) = \frac{1}{sc_g} i_{g\alpha\beta}(s), \tag{3}$$

Considering that the transfer function of (3), and the implementation of the voltage control algorithm on the stationary reference frame, the choice of the controller polynomials are $Q_m(s) = s^2+\omega_g^2$, $L(s) = 1$ and $P(s) = a_2s^2+a_1s+a_o$, which results in the following transfer function [27]

$$R_v(s) = \frac{a_2s^2 + a_1s + a_0}{s^2 + \omega_g^2}, \tag{4}$$

where a_2, a_1, and a_0 are the controller gains, and ω_g is the nominal frequency of the power grid. The use of the proposed voltage regulator determines the following characteristic polynomial for the GF-PC output voltage

$$A_v(s) = s^3 + \frac{a_2}{c_g}s^2 + \frac{(c_g\omega_g^2 + a_1)s}{c_g} + \frac{a_o}{c_g}. \tag{5}$$

Based on this approach, the suitable closed-loop poles of GF-PC voltage control loop can be assigned to those of the Hurwitz polynomial $A^*_v(s)$, expressed by

$$A^*_v(s) = (s^2 + 2\xi_v\omega_{nv}s + \omega_n^2)(s + \kappa\xi_v\omega_{nv}), \tag{6}$$

where ξ_v and ω_{nv} are the design damping ratio, and natural frequency of the standard second-order system and $-\kappa\xi_v\omega_{nv}$ is the position of a non-dominant pole. The polynomial of (6) can be rewritten as

$$A^*_v(s) = s^3 + \lambda^*_2s + \lambda^*_1s + \lambda^*_o, \tag{7}$$

in which $\lambda^*_2 = \xi_v\omega_{nv}(2+\kappa)$, $\lambda^*_1 = \omega^2_{nv}(1+2\kappa\xi_v^2)$, and $\lambda^*_o = \kappa\xi_v\omega^3_{nv}$. By solving the Diophantine equation for the Hurwitz polynomial $A^*_v(s)$, the gains of the voltage controller can be determined as

$$a_2 = c_g\lambda^*_2a_1 = c_g(\lambda^*_1 - \omega_g^2)\ a_o = c_g\lambda^*_o \tag{8}$$

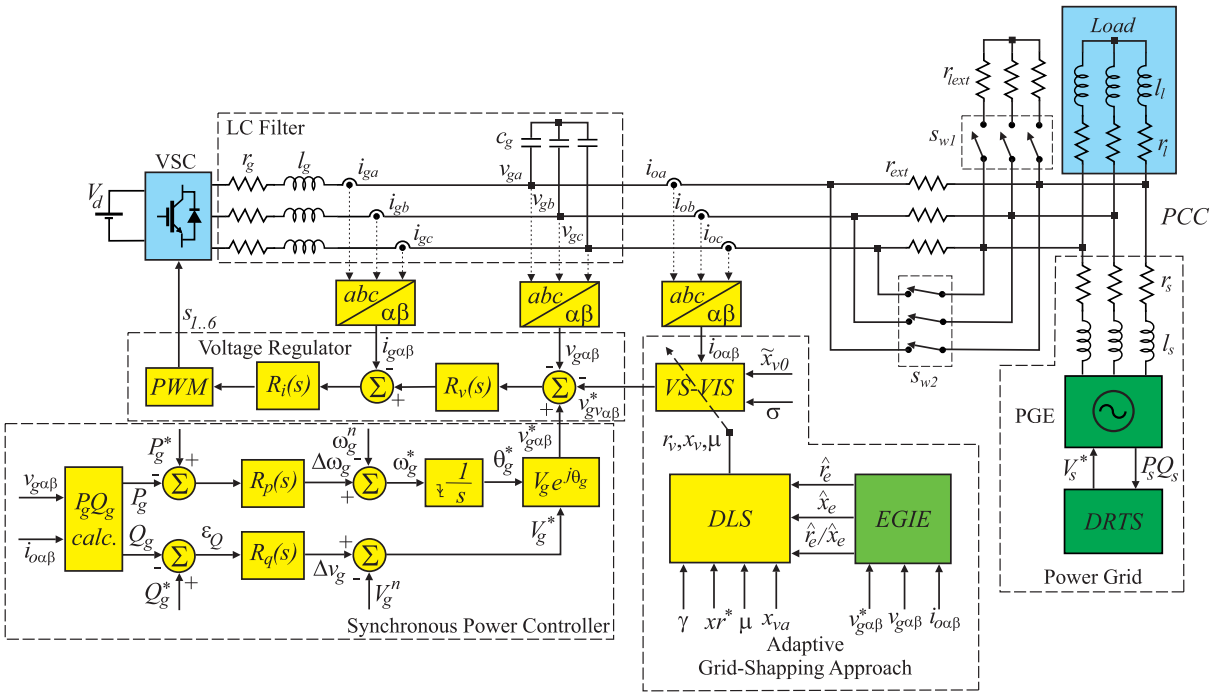

FIGURE 1. Block diagram of the GF-PC laboratory setup including; power grid, testing setup, GF-PC control system, and adaptive grid-shaping approach.

When a P controller regulates the LC input currents, the GF-PC output voltages ($v_{g\alpha\beta}(s)$) can be expressed in terms of $i^*_{g\alpha\beta}(s)$ as [26]

$$v_{g\alpha\beta}(s) = \frac{k_{pi}}{c_g l_g s^2 + c_g(r_g + k_{pi})s + 1} i^*_{g\alpha\beta}, \tag{9}$$

where c_g, l_g, and r_g are the parameters of the LC filter depicted in Fig. 1, and k_{pi} is the proportional gain of the current regulator. From (9), the damping factor and natural frequency can be given by $\xi_i = c_g(r_g + k_{pi})/(2\sqrt{c_g l_g})$ and $\omega_{ni} = \sqrt{1/(c_g l_g)}$, respectively.

The LC filter determines the natural frequency, while the gain k_{pi} can be used to adjust the required system damping. Better damping conditions can be achieved with a higher k_{pi} value, which increases the system phase shift [26]. Because of this, an interactive tuning procedure is employed to achieve the control objectives. In this method, the definition of the desired characteristic polynomial $A^*_v(s)$ accomplishes the compensation of the phase shift of the current control loop at the operating frequency [26].

B. ACTIVE AND REACTIVE POWER CONTROL LOOPS

The implementation of the proposed grid-forming converter's active and reactive power control strategies follows the synchronous power controller (SPC) proposed in [28], according to the block diagram in Fig. 1. The SPC control strategy regulates the delivered active and reactive powers by adjusting the amplitude and the phase angle of GF-PC output voltage, similar to the synchronous generator. Moreover, the SPC employs a virtual impedance approach to achieve the required X/R ratio with an inductive profile.

Conventionally, the exchange of active and reactive power that occurred between two voltage sources, v_g and v_s, can be written as

$$P_g = \frac{V_g V_s}{Z_s}\cos(\phi_s - \theta_g) - \frac{V_s^2}{Z_s}\cos(\phi_s), \tag{10}$$

$$Q_g = \frac{V_g V_s}{Z_s}\sin(\phi_s - \theta_g) - \frac{V_s^2}{Z_s}\sin(\phi_s), \tag{11}$$

where V_g and V_s are the root-mean-square (RMS) of instantaneous voltages of the grid-forming converter v_g, and the power grid v_s, $Z\angle\phi_s$ is the interconnection impedance, and θ_g is the phase angle between v_g and v_s. When the interconnection impedance has an inductive profile with a small value of θ_g, (10) and (11) become

$$P_g \approx \frac{V_g V_s}{X_s}\theta_g = W_p\theta_g, \tag{12}$$

$$Q_g \approx \frac{V_g}{X_s}\left(V_g - V_s\right) = W_q\Delta V. \tag{13}$$

where $W_p = V_g V_s/X_s$, $W_q = V_g/X_s$, $\Delta V = V_g - V_s$, and X_s is the reactance related to Z_s. Figs. 2(a) and 2(b) present the block diagrams of the linear model of the active and reactive power control loops. In this diagram, first-order low-pass filters (LPF) with cutoff frequency ω_f are employed in the system power measurements, and controllers $R_p(s)$ and $R_q(s)$ regulate the active and reactive powers.

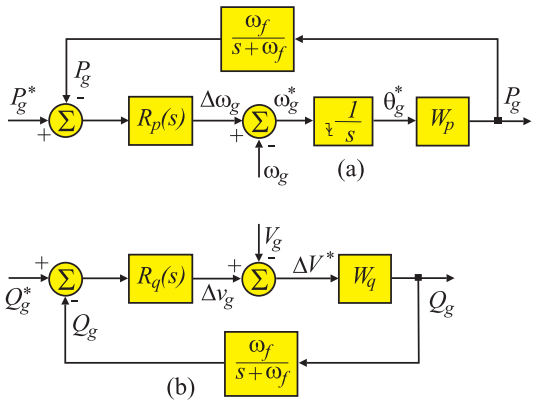

FIGURE 2. Block diagram of small-signal models of (a) active and (b) reactive control loops in Fig. 1.

1) ACTIVE POWER CONTROL LOOP

The active power control loop employs a configurable natural droop regulator (CNDR) proposed in [28], implemented based on a standard proportional-integral (PI) controller, with the inclusion of a parallel branch for providing the system $P-f$ droop slope. The transfer function of the CNDR controller is given by

$$R_p(s) = \frac{k_{pp}s + k_{ip}}{s + k_{gp}}, \tag{14}$$

where k_{pp}, k_{ip}, and k_{gp} are the controller gains, with k_{gp} being used to configure the system $P-f$ droop behavior. Substituting the CNDR controller in Fig. 2(a) by using Eq. (14), the resulting closed-loop transfer function can be expressed as

$$P_g(s) = \frac{\left(2\xi_p\omega_{np} - k_{gp}\right)s + \omega_{np}^2}{s^2 + 2\xi_p\omega_{np}s + \omega_{np}^2}P_g^*(s), \tag{15}$$

in which the damping coefficient ξ_p and natural frequency ω_{np} are given by

$$\xi_p = \frac{W_p k_{pp} + k_{gp}}{2\omega_{np}}, \tag{16}$$

$$\omega_{np} = \sqrt{W_p k_{ip}}, \tag{17}$$

The pole inserted by LPF used in power measurements can be considered as non-dominant due to the conventional criteria for setting its cutoff frequency ω_f [29]; for that reason, it is neglected in Eq. (15).

The $P-f$ droop response for the active power control loop can also be obtained from the analysis of the dynamic model depicted in Fig. 2(a) and can be expressed as

$$\frac{\Delta P_g(s)}{\Delta\Omega_g(s)} = \frac{-W_p(s + k_{gp})}{s^2 + 2\xi_p\omega_{np}s + \omega_{np}^2}. \tag{18}$$

in which the steady-state value of (18) depicts the controller the $P-f$ droop slope that is given by

$$D_p = \frac{\omega_g k_{gp}}{S_r k_{ip}}, \tag{19}$$

where the ω_g is the nominal angular speed of the power grid and S_r is the nominal power of the grid-forming converter.

Different design criteria can be employed to set up the CNDR's controller gains to perform the system's required dynamic behavior. According to [28], the integral gain k_{ip} can be determined in terms of suitable inertia needed for application as given

$$k_{ip} = \frac{\omega_g}{2HS_r}, \tag{20}$$

where H is inertia constant.

Since (20) has given the criterion to determine k_{ip}, the droop slope will only be determined by k_{gp} once k_{ip} has been fixed (i.e., according to Eq. (19)). Then the criterion to determine k_{gp} can be expressed as

$$k_{gp} = \frac{D_p}{2H}, \tag{21}$$

Finally, the proportional gain k_{pp} can be defined by substituting (20) and (21) in (16), which results in

$$k_{pp} = 2\xi_p\sqrt{\frac{\omega_g}{2HS_rW_p}} - \frac{D_p}{2HW_p}. \tag{22}$$

The control parameters k_{pp}, k_{ip}, and k_{gp}, can be set up according to the input of D_p, H, and ξ_p. Thus, a suitable design procedure can be performed if the link between the controller gains and the characteristic parameters has been established.

2) REACTIVE POWER CONTROL LOOP

A proportional-integral (PI) controller is employed in the reactive power control loop to properly adjust the grid-forming output voltage [30]. Different from the conventional droop, an integral controller is adopted for assuring the zero steady-state reactive power tracking in grid-tied operation. Furthermore, when the grid-forming operates under islanding conditions, the integral gain of the PI controller should be fixed to zero [30].

The closed-loop transfer function of the reactive power can be obtained from Fig. 2(b), substituting in $R_q(s)$ block the standard PI controller transfer function, which results in

$$Q_g(s) = \frac{W_q\left(k_{pq}s + k_{iq}\right)(s + \omega_f)}{s^2 + 2\xi_q\omega_{nq}s + \omega_{nq}^2}Q_g^*, \tag{23}$$

in which, the damping coefficient ξ_q and ω_{np} are given by

$$\xi_q = \frac{\omega_f\left(1 + W_q k_{pq}\right)}{2\omega_{nq}}, \tag{24}$$

$$\omega_{nq} = \sqrt{W_q\omega_f k_{iq}}, \tag{25}$$

where k_{pq} and k_{iq} are the controller gains.

Unlike the active power control strategy, the LPF used in the power measurements is considered in the reactive power control loop modeling. Its insertion provides more freedom degrees to set up the PI controller parameters to achieve suitable transient and steady-state performance [31].

In summary, the PI controller operates as a droop + integral controller, in which the proportional gain (k_{pq}) configures the $Q - V$ droop slope, and the integral part (k_{iq}/s) mitigates the steady-state error for grid-connected operation [32]. First, the network standards associated with the power converter characteristics are used to determine the suitable droop coefficient k_{pq}. Then, the integral gain k_{iq} can be defined considering the required transient and steady-state performance and the LPF filter cutoff frequency ω_f.

III. ADAPTIVE GRID IMPEDANCE SHAPING APPROACH

The synchronous power control (SPC) control employed in this work requires a feeder impedance with an inductive profile to provide its main features. Because of this, an adaptive virtual impedance shaping approach is proposed based on a variable structure virtual impedance strategy (VS-VIS). Its implementation comprises the following modules:

- Equivalent grid impedance estimator,
- Decision logic system, and
- Variable structure virtual impedance strategy.

These modules are implemented by the blocks EGIE, DLS, and VS-VIS in Figs. 1. Their functionalities and how their integration adaptively shapes the system's equivalent grid impedance with the required X/R ratio to perform an inductive profile are described next.

A. EQUIVALENT GRID IMPEDANCE ESTIMATION - EGIE

The standard power flow equations estimate the feeder equivalent impedance when PCC voltage and power parameters are known. However, GF-PC control strategies only employ output voltage and power information to provide the required power flow control, making it impossible to estimate the PCC equivalent impedance. Nonetheless, the insertion of PCC current sensors (i.e., PCC current sensors $i_{o\alpha\beta}$ in Fig. 1) can provide the required power information, enabling the PCC equivalent impedance estimation [8]. Although, this calculation procedure does not include the virtual impedance insertion. For that reason, in this work, the reference voltages of GF-PC's control system ($v^*_{g\alpha\beta}$) are also included for providing the required equivalent impedance estimation with the virtual impedance implementation. To achieve this required estimation procedure considers that the system's overall power, composed of local measurements and control set-points, can be calculated as follows

$$\begin{cases} P_c = \delta v_{c\alpha} i_{o\alpha} + \delta v_{c\beta} i_{o\beta}, \\ Q_c = \delta v_{c\beta} i_{o\alpha} - \delta v_{c\alpha} i_{o\beta}, \end{cases} \tag{26}$$

where P_c and Q_c are the GF-PC's overall power, $\delta v_{c\alpha\beta} = v^*_{g\alpha\beta} - v_{g\alpha\beta}$ is the voltage difference between the reference and GF-PC output voltages, and $i_{o\alpha\beta}$ is the PCC current measurement. Low-pass filters mitigate the switching frequency in the P_c and Q_c power calculations.

Considering that the system is symmetrical and balanced, the module of their equivalent impedance can be estimated by

$$\widehat{z}_e = \frac{V^*_{g\alpha}}{I_{o\alpha}} = \frac{V^*_{g\beta}}{I_{o\beta}}, \tag{27}$$

where $V^*_{g\alpha\beta}$ and $I_{o\alpha\beta}$ are the root-mean-square (RMS) values of the GF-PC reference voltages ($v^*_{g\alpha\beta}$) and PCC currents ($i_{o\alpha\beta}$) respectively. The resistance and reactance components of the equivalent impedance ($\widehat{z}_e$) refer to its real and imaginary parts that can be determined as

$$\widehat{r}_e = \frac{\widehat{z}_e P_c}{S_c}, \tag{28}$$

$$\widehat{x}_e = \frac{\widehat{z}_e Q_c}{S_c}, \tag{29}$$

where $S_c = \sqrt{P_c^2 + Q_c^2}$ is the apparent power related to the system equivalent impedance.

The block EGIE in Fig. 1 estimates $\widehat{z}_e$ by using the Eqs. (26)-(29). Then, it is decomposed into resistive and inductive parts ($\widehat{r}_e$ and $\widehat{x}_e$), allowing the evaluation of the X/R feeder ratio. This procedure is only suitable for grid-connected operations. When the GF-PC operates on islanded conditions, the grid impedance approach is disabled.

B. DECISION LOGIC SYSTEM - DLS

The decision logic scheme (Block DLS in Fig. 1) defines the virtual impedance profile and its components values to reach the desired X/R ratio based on the grid impedance estimation ($\widehat{z}_e = \widehat{r}_e + j\widehat{x}_e$) and converter power availability. The virtual impedance implementation employs an RL branch composed of a virtual negative resistance, which is series connected with a virtual inductance. The value of virtual resistance is determined by using a reduction factor γ, given as follows

$$r^*_v = r_v = -\gamma \widehat{r}_e, \tag{30}$$

where γ is constrained in $0 \leq \gamma \leq 1$. The maximum value of γ can be determined considering the suitable damping condition of the network that interconnects the application. The value of the virtual inductive reactance is calculated as a function of r^*_v and the desired X/R ratio (specified by the parameter xr^*), which can be expressed as

$$x^*_v = xr^* \, |r_v| - \widehat{x}_e, \tag{31}$$

considering the condition $xr^* \geq 10$ for guaranteeing the power decoupling, from the analysis of (10) and (11), considering $X_s = 10R_s$, which results in the approximation depicted by (12) and (13).

The maximum value of the virtual reactance is restricted to the power availability of the grid-connected power converter to assure the feasibility of the grid shaping procedure, which is given by

$$x_{va} = \frac{3V_g^2}{\sqrt{S_r^2 - P_g^2}}, \tag{32}$$

where P_g is the converter power delivery, and V_g is the RMS value of the power grid nominal voltage. Therefore, to guarantee the feasibility of the proposed grid shaping approach, the virtual reactance must be restricted to $x_v^* < x_{va}$.

The DLS also employs an updating mechanism to mitigate transients during the virtual reactance implementation. In this procedure, the estimates $\widehat{r}_e(t)$ and $\widehat{x}_e(t)$ as well as the virtual reactance setpoint $x_v^*(t)$ of two subsequent sampling times (t_{k-1} and t_k) are stored. The estimations of grid impedance components are employed to evaluate the X/R deviation, which can be calculated as follows

$$\Delta xr(t_k) = \frac{\widehat{x}_e}{\widehat{r}_e}(t_k) - \frac{\widehat{x}_e}{\widehat{r}_e}(t_{k-1}). \tag{33}$$

This deviation is compared with the maximum allowed X/R variation defined as

$$\Delta xr_{\max} = \mu xr^*(t_{k-1}), \tag{34}$$

where μ is a constant restricted in $0 \leq \mu \leq 1$. The value of $\Delta xr_{\max}$ must be chosen based on the allowed PCC voltage variation, considering the standard specifications [33]. The value of x_v that must be implemented to reach the desired X/R can be defined as

$$\begin{cases} if\,(|\Delta xr(t_k|) \geq \Delta xr_{\max}) \Longrightarrow x_v = x_v^*(t_k), \\ if\,(|\Delta xr(t_k|) < \Delta xr_{\max}) \Longrightarrow x_v = x_v^*(t_{k-1}), \end{cases} \tag{35}$$

where $x_v^*(t_{k-1})$ and $x_v^*(t_k)$ are the virtual reactance setpoints determined according to (31) for the sampling times t_{k-1} and t_k, stored previously.

This procedure generates a dead zone delimited by $(\widehat{x}_e/\widehat{r}_e)(t_k) - \Delta xr_{\max}$ and $(\widehat{x}_e/\widehat{r}_e)(t_k) + \Delta xr_{\max}$, in which X/R variations inside this interval do not update the value of reactance to be implemented. Inside this dead zone, a fine-tuning procedure based on a non-linear control approach is employed to match the required X/R for promoting the PQ decoupling. Besides, this mechanism avoids transients provoked by abrupt virtual impedance control actions to compensate for sudden grid impedance deviations.

C. VARIABLE STRUCTURE VIRTUAL IMPEDANCE STRATEGY - VS-VIS

The grid impedance shaping scheme is based on a VS-VIS composed of the association of a standard linear approach and a sliding-mode control (SMC) strategy developed from the methodology proposed in [25]. In this scheme, the virtual resistance r_v^* implementation employs a linear approach while the virtual reactance x_v uses a variable structure composed of linear and SMC techniques, in which x_v is decomposed into two parts, given by

$$\overline{x}_v = (1-\mu)x_v, \tag{36}$$

$$\widetilde{x}_v = \mu x_v, \tag{37}$$

where $\overline{x}_v$ is implemented using a linear approach and $\widetilde{x}_v$ employs an SMC scheme.

The definition of μ is based on the expected grid impedance deviation, which results in $\overline{x}_v > \widetilde{x}_v$, making $\overline{x}_v$ dominant to match the X/R control objectives. Therefore, $\overline{x}_v$ provides the major part of the required reactance, and $\widetilde{x}_v$ produces a fine-tuning action inside the dead zone depicted by (35) by using the SMC main features for compensating unmodeled disturbances [25].

1) SLIDING-MODE VIRTUAL IMPEDANCE APPROACH

The sliding mode methodology employed for implementing the virtual impedance $\widetilde{x}_v$. According to the block diagram of Fig. 2, the relationship between the reactive power (Q_g) and the voltage deviation (Δv_g) can be established as follows

$$\left(Q_g^* - \frac{\omega_f}{s+\omega_f}Q_g\right)\left(\frac{k_{pq}s + k_{iq}}{s}\right) = \Delta v_g, \tag{38}$$

where ω_f is the cutoff frequency of the low-pass filter employed in the GF-PC power measurement.

Defining the state-variable $x_1 = Q_g^* - Q_g$, with $x_2 = \dot{x}_1$, and introducing a control input u_{eq}, the state-space system related to the sliding mode virtual impedance (SM-VI), can be derived from Eq. (38), which results in

$$\begin{cases} \dot{x}_1 = x_2 \\ \dot{x}_2 = -\omega_f x_2 - \dfrac{\omega_f k_{iq}}{k_{pq}}x_1 + d(t) + \dfrac{1}{k_{pq}}u_{eq}, \end{cases} \tag{39}$$

with u_{eq} given by:

$$u_{eq} = -ax_2 - LPF(\beta_0 sgn(\sigma)), \tag{40}$$

where $\beta_0 = \widetilde{x}_v + \widetilde{x}_{v0}$, in which $\widetilde{x}_{v0} > 0$ is the initial value of reactance that assures the required reaching time to the sliding surface, $LPF(\cdot)$ is a first-order low-pass filter used to mitigate the SMC chattering, and $sgn(\cdot)$ is a signum function that is defined as follows

$$sgn(\sigma) = \begin{cases} -1 & if\ \sigma < 0 \\ 0 & if\ \sigma = 0, \\ 1 & if\ \sigma > 0 \end{cases} \tag{41}$$

and σ is the sliding manifold given by

$$\sigma = ax_1 + x_2, \tag{42}$$

where a is the SMC controller gain.

The value of $\widetilde{x}_v$ to assure the SM-VI stability and guaranteeing the required reactive power-sharing must satisfy the following inequality

$$\left|\frac{k_{pq}(a-\omega_f)x_2 - \omega_f k_{iq}x_1 + d(t)}{I_g}\right| \leq \widetilde{x}_v. \tag{43}$$

The analysis of Eq. (43) is effectuated by considering the inequality upper bound addresses the following simplification

$$\widetilde{x}_v \geq \frac{\omega_f k_{iq}}{|I_g|}|x_1| \cong \frac{\omega_f k_{iq}}{|I_g|}\Delta Q_v, \tag{44}$$

where ΔQ_v is the amount of reactive power required to provide the fine-tuning inside the dead zone defined in (35). Admitting that the system is under convergence

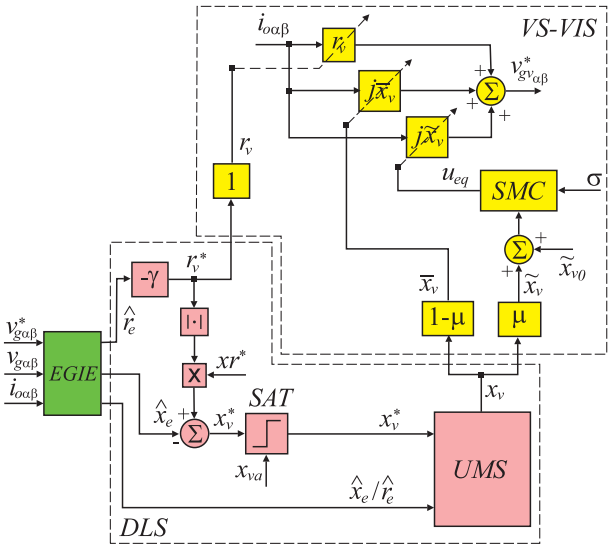

FIGURE 3. Block diagram of adaptive grid impedance shape implementation.

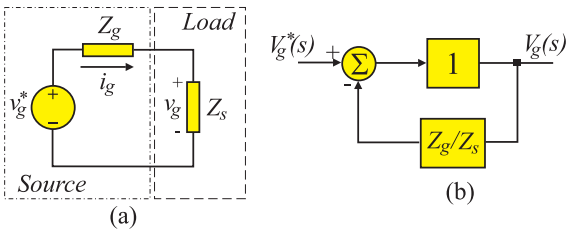

FIGURE 4. (a) equivalent circuit of the GF-PC interconnected to the PCC, and (b) feedback control system.

(i.e., $|\sigma| = 0$), the trajectories must reach the sliding manifold in the finite time determined by

$$t_r \leq \frac{k_{pq}|\sigma(0)|}{\widetilde{x}_{v0}|I_g|}, \tag{45}$$

where $|\sigma(0)|$ is the upper bound of the system's initial condition. Therefore, the suitable value of $\widetilde{x}_{v0}$ is designed to compensate for the bounded disturbance of grid impedance (i.e., estimated as $\Delta xr_{\max}$), and SMC controller gain a is responsible for determining the sliding surface reaching time t_r.

D. IMPLEMENTATION OF ADAPTIVE GRID IMPEDANCE SHAPING APPROACH

The implementation of the proposed adaptive grid shaping approach is depicted in Fig. 3, in which the following steps summarize the main control actions:

1) The module EGIE estimates $\widehat{r}_e$ and $\widehat{x}_e$, in real-time, using (26)-(29).
2) Given the estimates $\widehat{r}_e$ and $\widehat{x}_e$, the DLS calculates r_v^* and x_v^* using (30) and (31), based on the setups γ and xr^*, suitable to perform the desired X/R ratio of the grid feeder.
3) Then, DLS evaluates if the implementation of x_v^* is feasible considering the GF-PC power availability defined by $x_v^* < x_{va}$, in which x_{va} is defined by (32).
4) The SAT block in the DLS module limits the maximum values of x_v^* in x_{va} when the condition $x_v^* < x_{va}$ is infringed.
5) The estimates $\widehat{r}_e(t)$ and $\widehat{x}_e(t)$ as well as the virtual reactance setpoint $x_v^*(t)$ of two subsequent sampling times (t_{k-1} and t_k) are stored, and the feeder X/R deviation is evaluated using (33).
6) The UMS compares $\Delta xr(t_k)$ with the maximum allowed X/R variation $\Delta xr_{\max}$ that is defined in (34) and implements the updating rule depicted in (35) to define x_v, using the stored values of $x_v^*(t)$ in samples t_{k-1} and t_k.
7) According to (36) and (37), the VS-VIS decomposes x_v into two parts, resulting in $\overline{x}_v$ and $\widetilde{x}_v$.
8) Virtual impedance components r_v and $\overline{x}_v$ are implemented using the standard linear approach according to the block diagram in Fig. 3 to synthesize the major part of the virtual impedance required to reach the X/R control objectives.
9) Simultaneously with step 8, the $\widetilde{x}_v$ is implemented through the SMC approach (40) and added to $r_v + j\overline{x}_v$ to reach the X/R control objectives that provided the required PQ decoupling.

The steps above depict the algorithm to execute the control actions required to implement the proposed adaptive grid shaping strategy. They comprise simple mathematical and logical operations, significantly reducing implementation complexity and computational burden.

E. IMPEDANCE-BASED STABILITY ANALYSIS

The impedance-based analysis follows the methodology proposed in [34], [35], in which the Nyquist stability criterion is applied to the minor loop gain defined by the internal impedance ratio between the GF-PC and the PCC (i.e., $Z_g(s)/Z_s(s)$), similarly to the loop gain of the feedback control system [35].

Fig. 4(a) and 4(b) present the equivalent circuit of the interconnection of the GF-PC (represented by the voltage source v_g^* series connected with Z_g) with the PCC (represented by the load Z_s) and the block diagram of the feedback control system, respectively.

According to the Nyquist theory, the stability criterion requires that the number of the counterclockwise encirclement of open-loop transfer function locus to the point $-1 + j0$ must be equal to the number of the right-half-plane (RHP) poles of the minor loop gain. Also, Middlebrook [36] reported a sufficient but more than necessary condition for the system stability that $\left|Z_g(s)/Z_s(s)\right| \ll 1$.

According to the Fig. 1, the dynamic behavior of GF-PC output voltage can be described as follows

$$V_{g\alpha\beta}(s) = G_v(s)V^*_{g\alpha\beta}(s) - Z_g(s)I_{o\alpha\beta}(s), \tag{46}$$

where $G_v(s)$ is the closed-loop transfer function of the GF-PC output voltage, and $Z_g(s)$ is the GF-PC output impedance. The

transfer function $G_v(s)$, considering the controller $R_v(s)$ in (4), is given by

$$G_v(s) = \frac{a_2 s^2 + a_1 s + a_0}{c_g s^3 + a_2 s^2 + (a_1 + \omega_g^2)s + a_0}, \quad (47)$$

in which $Z_g(s)$ without the virtual impedance implementation is expressed as

$$Z_g(s) = \frac{s^2 + \omega_g^2}{c_g s^3 + a_2 s^2 + (a_1 + \omega_g^2)s + a_0}. \quad (48)$$

When the virtual impedance is implemented, the original reference voltage $V^*_{g\alpha\beta}(s)$ is modified by the following a droop function

$$V^{*'}_{g\alpha\beta}(s) = V^*_{g\alpha\beta}(s) - Z_v(s) I_{o\alpha\beta}(s), \quad (49)$$

where $Z_v(s)$ is the virtual impedance to be implemented. Considering that $Z_v(s)$ is defined as $z_v = r_v + s l_{vt}$, the $Z_g(s)$ becomes

$$Z_g(s) = \frac{z_3 s^3 + z_2 s^2 + z_1 s + z_0}{c_g s^3 + a_2 s^2 + (a_1 + \omega_g^2)s + a_0}, \quad (50)$$

with $z_3 = a_2 l_{vt}$, $z_2 = a_2 r_v + a_1 l_{vt} + 1$, $z_1 = a_1 r_v + a_0 l_{vt}$, and $z_0 = a_0 r_v + \omega_g^2$, where a_2, a_1, and a_0 are the gains of the controller $R_v(s)$ according to (4); r_v, and l_{vt} are the values of virtual resistance and virtual inductance.

The value of l_{vt} is associated with the virtual reactance (i.e., $l_{vt} = x_{vt}/\omega_g$) composed of two parcels ($x_{vt} = \bar{x}_v + \widetilde{x}_v$), defined using (36) and (37). The implementation of the SMC virtual impedance employs the control law of (40), implemented using a relay that switches between $\pm\beta_0 = \widetilde{x}_v + \widetilde{x}_{v0}$, commanded by the signum function sgn(·) defined in (41). In addition, a first-order low-pass filter mitigates the SMC chattering, resulting in the control input u_{eq}.

It is necessary to obtain the minor loop gain defined by the impedance ratio $Z_g(s)/Z_s(s)$ to apply the Nyquist impedance-based stability to the proposed GF-PC. Considering that the output impedance of the PCC is $Z_s(s) = r_s + j l_s$, the impedance ratio $Z_g(s)/Z_s(s)$ can be expressed as

$$\frac{Z_g(s)}{Z_s(s)} = \frac{z_3 s^3 + z_2 s^2 + z_1 s + z_0}{w_4 s^4 + w_3 s^3 + w_2 s^2 + w_1 s + w_0}, \quad (51)$$

where $w_4 = l_s c_g$, $w_3 = r_s[c_g + l_s(w_g^2 c_g + a_2)]$, $w_2 = r_s\left(l_s a_1 + w_g^2 c_g + a_2\right)$, $w_1 = r_s\,(a_1 + l_s a_0)$, and $w_0 = r_s a_0$.

The transfer function (51) keeps the same numerator of (50) but presents a characteristic polynomial with an increased order due to the PCC output impedance insertion.

The impedance-based analysis uses the following operational scenarios: (i) Compensation of grid resistance increasing, and (ii) Compensation of grid inductance reduction.

The $R_v(s)$ controller gains employed in both operational scenarios follow the design methodology of Section II-A, while the grid-shaping approach is configured to reach $X/R = 10$. Besides, the maximum values of the SMC switching function (i.e., $\pm\beta_0 = \widetilde{x}_v + \widetilde{x}_{v0}$) are used to increase its implementation severity. Therefore, two polar plots related to $+\beta_0$ and $-\beta_0$ are presented in each study.

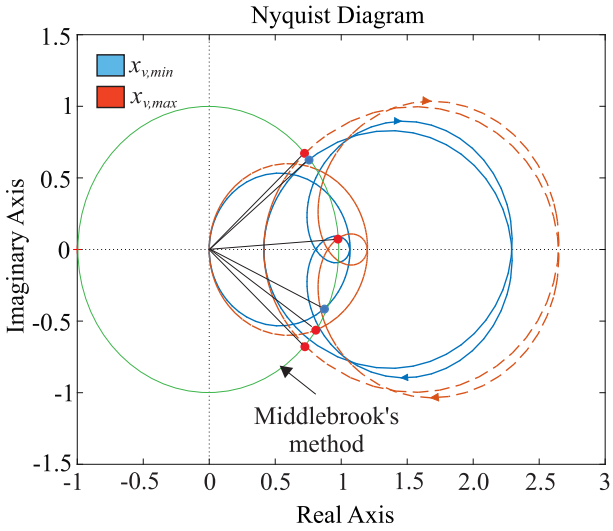

FIGURE 5. Polar plot of minor loop gain of grid-shaping procedure applied for operational scenario 1.

1) SCENARIO 1 - COMPENSATION OF GRID RESISTANCE INCREASING WITH $X/R = 10$

Fig. 5 presents the polar plot of Nyquist analysis of the minor loop gain of Scenario 1, in which the grid resistance is increased from $r_s = 0.4\ \Omega$ to $r_s = 0.8\ \Omega$, keeping the grid inductance in $l_s = 3.6$ mH. As a result, the grid reactance is $x_s \approx 1.31\ \Omega$, considering the network nominal $f_g = 50$ Hz, corresponding to $X/R \approx 1.635$. According to grid-shaping design criteria, the equivalent resistance must be reduced by 50%, resulting in $r_v = -0.4\ \Omega$. Therefore, it is necessary a virtual reactance of $x_v \approx 2.69\ \Omega$ (i.e., $l_v = 8.6$ mH) to reach $X/R = 10$. According to the proposed methodology, the value of x_v is decomposed into $\bar{x}_v \approx 2.152\ \Omega$ and $\widetilde{x}_v = 0.538\ \Omega$, respectively.

The insertion of the SMC behavior in the Nyquist analysis is performed using $x_{vt} = \bar{x}_v \pm \Delta x_v$, in which $\Delta x_v \approx 0.726\ \Omega$ for accomplishing the insertion of the initial value $\widetilde{x}_{v0}$. These two conditions are more severe than the SMC implementation since its output u_{eq} corresponds to $\widetilde{x}_v$ average value due to the use of the LPF filter in the SMC control law (40).

Analyzing the two polar plots of Fig. 5, described by the red and blue lines (i.e., $x_{v,\max}$ and $x_{v,\min}$ in Fig. 5), it is possible to observe that both graphs do not encircle the point $-1 + j0$, which guarantees the system stability for these operational conditions.

2) SCENARIO 2 - COMPENSATION OF GRID INDUCTANCE REDUCTION WITH $X/R = 10$

In this case, the grid resistance returns to $r_s = 0.4\ \Omega$ (standard value), and the grid inductance is reduced from $l_s = 3.6$ mH to $l_s = 2.4$ mH, reaching the $X/R \approx 1.885$. The required virtual reactance to achieve the control objective $X/R = 10$ is $x_{vt} \approx 1.246\ \Omega$ (i.e., which corresponds to $l_{vt} \approx 4$ mH for $f_g = 50$ Hz.). Similar to the previous study, the virtual reactances is split into $\bar{x}_v = 0.996\ \Omega$ and $\widetilde{x}_v = 0.242\ \Omega$, and the reactances

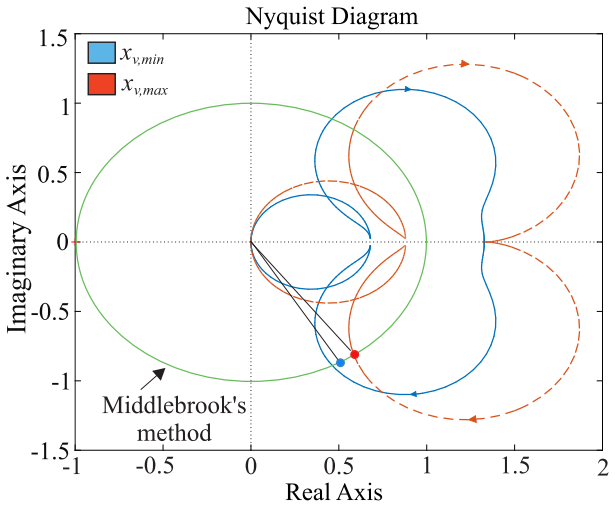

FIGURE 6. Polar plot of minor loop gain of grid-shaping procedure applied for operational scenario 2.

employed in the stability study are defined as $x_{vt} = \bar{x}_v \pm \Delta x_v$, with $\Delta x_v \approx 0.437\ \Omega$. Fig. 6 depicts the polar plots of the Nyquist stability analysis related to this operational scenario. Like the previous study, the two polar plots do not encircle the point $-1 + j0$, ensuring the system stability through the compensation of grid reactance reduction.

Finally, the Nyquist stability studies demonstrated that the design criteria adopted to set up the gains of the voltage regulator, associated with the design criteria applied for the proposed grid-shaping approach, assure the stability of the proposed method up to the physical limits of the power converter.

IV. EXPERIMENTAL RESULTS

The validation of the proposed control strategy employs a GF-PC laboratory setup implemented according to the block diagram depicted in Fig. 1. Table 1 presents the system parameters. A fast prototyping system, dSPACE1202, executes the control system and the adaptive grid impedance shaping algorithms, with a sampling rate of $T_s = 100\ \mu s$. Using antialiasing filters with a cutoff frequency of $F_c = 2.5$ kHz, Hall-effect sensors provide the system voltage and current measurements. This control scheme uses two sets of current sensors to estimate the required grid impedance (i.e., one set for measuring the LC filter inductors currents and another for the GF-PC output currents). The second set can be substituted by a simple estimation scheme based on the LC filter model and output voltage measurements. The proposed method was tested in the following scenarios:

- System operation without grid shaping system,
- Operation with adaptive grid impedance shaping,
- Step variations of virtual resistance and reactance.
- Compensation for grid impedance variation, and
- Operation under PCC load variation.

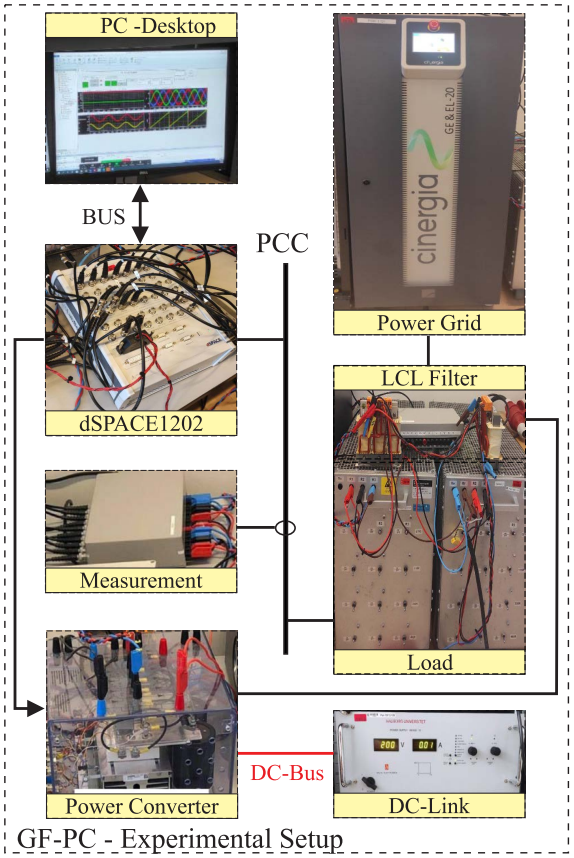

FIGURE 7. (Grid-forming laboratory experimental setup.

TABLE 1. GF-PC Laboratory Setup Parameters.

Par.	Val.	Par.	Val.
V_g	70 V(rms)	ω_g	100π rad/s
l_g	2.4 mH	r_g	0.2 Ω
c_g	15 μF	l_s	3.6 mH
r_s	0.4 Ω	V_d	200 V
k_{pp}	0.023	k_{ip}	0.0016
k_{pq}	0.00795	k_{iq}	0.0795
μ	0.2	a	1
γ	0.5	k_{pi}	1000
r_l	10 Ω	l_l	10 mH
r_{lext}	50 Ω	r_{ext}	0.06 Ω
ω_f	10 rad/s	F_c	2.5 kHz
T_s	100 μs	a_2	1.368
a_1	221.7811	a_0	135010.8

Fig. 7 shows the GF-PC experimental setup employed for validating the proposed adaptive grid impedance shaping method according to block diagram of Fig. 1.

A. STARTUP PROCEDURE AND SYSTEM OPERATION WITHOUT GRID SHAPING SYSTEM

Figs. 8(a)-8(e) present the experimental results related to the system startup procedure. First, the GF-PC is synchronized to the power grid with reference powers of $P_g^* = 70$ W and $Q_g^* = 100$ VAr. Then, when the system reaches the steady-state

condition, active and reactive power steps of $\Delta P_g = 830$ W and $\Delta Q_g = 200$ VAr are added to the P_g^* and Q_g^* setpoints at $t \approx 2.3$ s and $t \approx 6.8$ s, respectively. Figs. 8(a) and 8(b) present the controlled active and reactive power graphs during the startup procedure. These figures also present PCC voltage snapshots during the active and reactive power steps.

In this experiment, the block EGIE initiates the estimation the equivalent grid impedance simultaneously with the synchronization process, but their values are only used when the GF-PC delivers active power. Figs. 8(c) and 8(d) present the system equivalent resistance $\widehat{r}_e$ and reactance $\widehat{x}_e$ estimations. Without the grid shaping implementation, the equivalent system impedance depicts the average values of $\widehat{r}_e = 0.38\ \Omega$ and $\widehat{x}_e = 1.4\ \Omega$. Fig. 8(f) presents the X/R system ratio obtained from the grid impedance estimation corresponding to a power coupling condition, with $\widehat{x}_e/\widehat{r}_e \approx 3.5$. This ratio increases when the control system implements a reactive power step but keeps a similar coupling condition. The coupling condition produces overshoots when the active and reactive power steps are implemented, as demonstrated in Figs. 8(a) and 8(b).

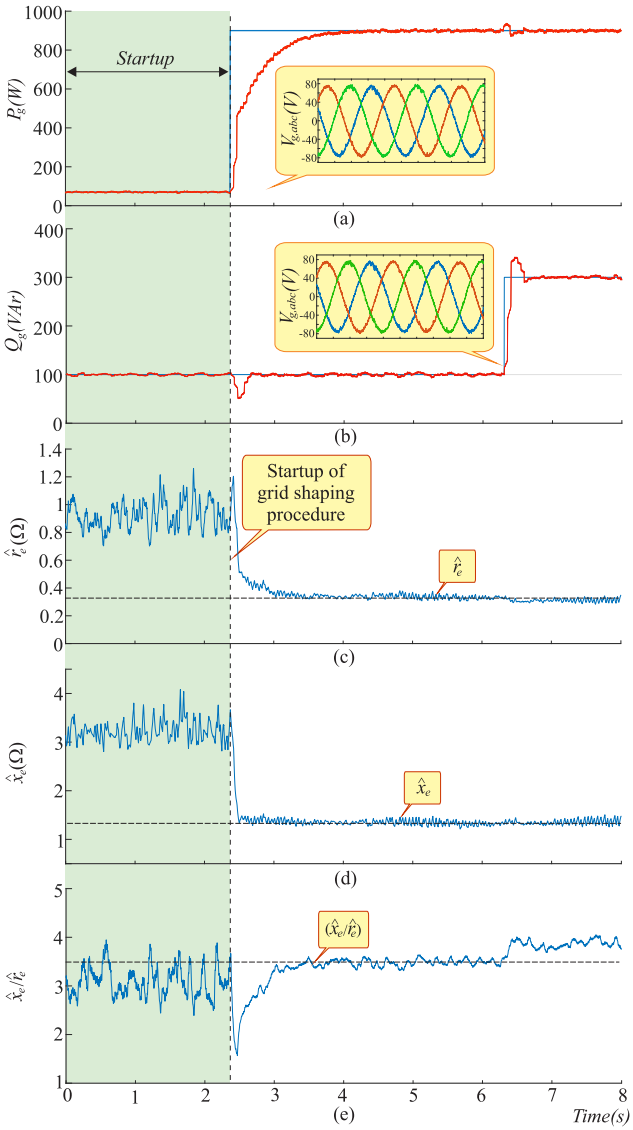

FIGURE 8. Experimental results of GF-PC without virtual impedance implementation; (a) active power delivered by GF-PC, (b) reactive power delivered by GF-PC, (c) equivalent resistance estimation, (d) equivalent reactance estimation, and (e) X/R ratio.

B. OPERATION WITH ADAPTIVE GRID IMPEDANCE SHAPING

Figs. 9(a)-9(f) show the experimental results of the proposed adaptive impedance shaping approach. After the beginning of active power injection, both conventional and SMC techniques implement the virtual impedance strategy with the adaptation technique depicted in Fig. 3. Figs. 9(a) and 9(b) illustrate the experimental results of the controlled active and reactive powers under the same conditions as the previous experiment. The overshoot occurrences due to the power step insertions are reduced compared with the test realized before, denoting the effectiveness of the proposed adaptive grid impedance shaping method.

Figs. 9(c) and 9(d) show the equivalent resistance and reactance obtained with the grid shaping procedure, which average values are $\widehat{r}_v \approx 0.18\ \Omega$ and $\widehat{x}_v \approx 2\ \Omega$, respectively. In this experiment, the X/R reference value of $xr^* \approx 14$ is adopted. As a result, the implemented virtual impedance depicts an estimated $\widehat{x}_e/\widehat{r}_e$ of approximately 13.8, as shown in Fig. 9(e). Furthermore, unlike the test before, with the implementation of the grid impedance shaping approach, the increase of system reactance is not verified during the reactive power step implementation. Finally, Fig. 9(f) presents the SMC virtual reactance $\widetilde{x}_v$ superimposed by its average value, in which the amplitude of the switching function is fixed $\beta_0 = 0.4\ \Omega$ for attending to the constraints of the stability condition (44) and reaching time (45).

C. STEP VARIATION OF VIRTUAL RESISTANCE AND SMC REACTANCE

Figs. 10(a) and 10(d) show the experimental results of the proposed VS-VIS using the virtual impedance components introduced separately. In this experiment, the system starts up without the virtual impedance and grid estimation schemes. Then, when the GF-PC starts delivering active power, both methods are implemented. During the startup procedure, the average values of the grid equivalent resistance, reactance, and X/R ratio are $\widehat{r}_e \approx 0.32\ \Omega$, $\widehat{x}_e \approx 1.4\ \Omega$, and $\widehat{x}_e/\widehat{r}_e \approx 4.4$, respectively. At $t \approx 3.2$ s, the VS-AVI inserts the fixed virtual reactance of $x_v = 0.8\ \Omega$ and the SMC reactance with switching function amplitude of $\beta_0 = 0.4\ \Omega$, as depicted in Figs. 10(b) and 10(d). The system X/R ratio increases from 4.1 to approximately 6.2, as presented in Fig. 10(c). Besides, a transient in the equivalent grid resistance estimation $\widehat{r}_e$ is observed, as shown in Fig. 10(a). At $t \approx 6.9$ s, the virtual resistance of $r_v = -0.2\ \Omega$ is implemented, reducing the grid equivalent value to $\widehat{r}_e \approx 0.14\ \Omega$, as shown in Fig. 10(a), increasing the system X/R ratio from 6.2 to approximately 14.2. Fig. 10(d) shows the SMC reactance implementation superimposed by its average value.

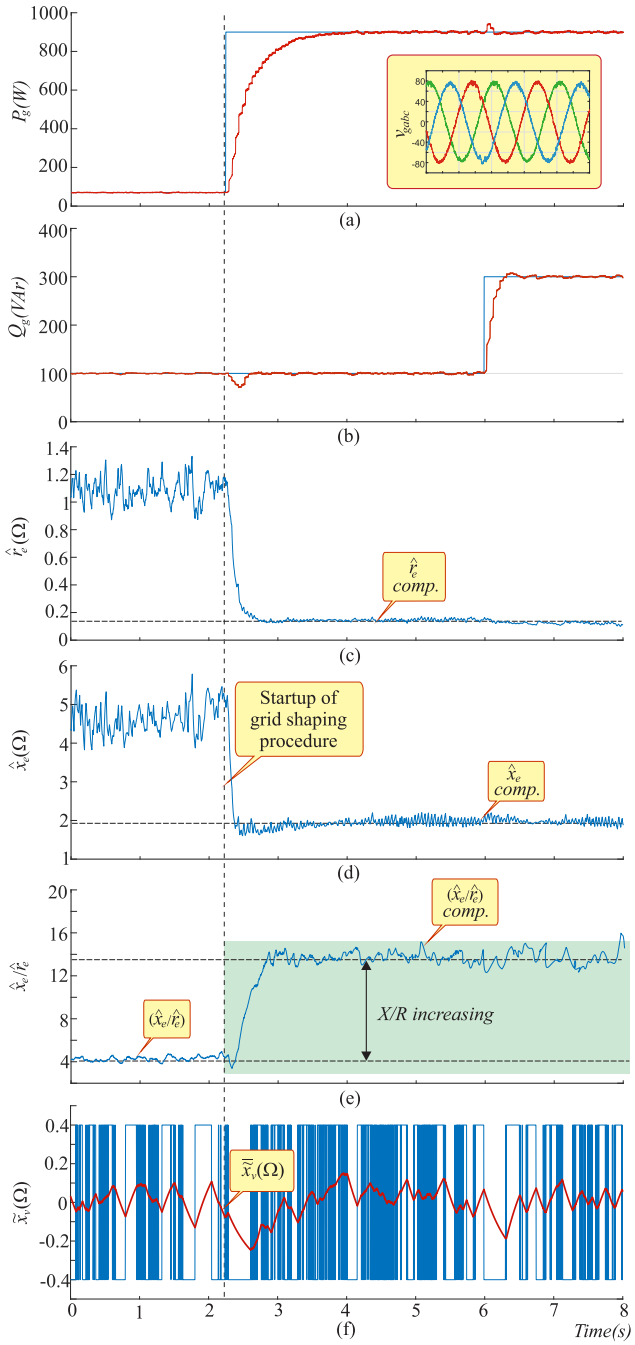

FIGURE 9. Experimental results of GF-PC with the proposed virtual impedance implementation; (a) active power delivered by GF-PC, (b) reactive power delivered by GF-PC, (c) equivalent resistance estimation, (d) equivalent reactance estimation, (e) X/R ratio, and (f) SMC reactance superimposed by its average value.

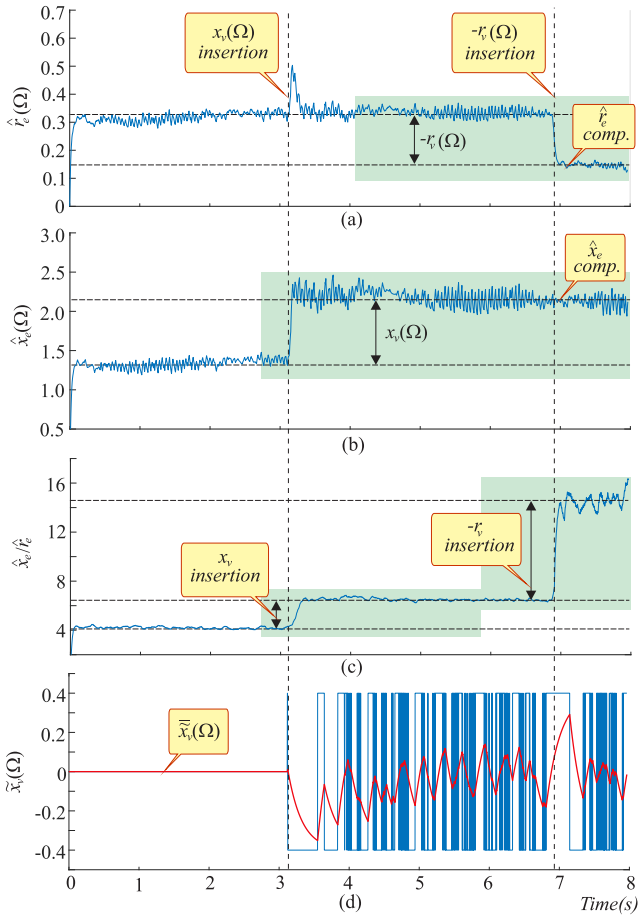

FIGURE 10. Experimental results of GF-PC under step variation of virtual impedance elements; (a) equivalent resistance estimation, (b) equivalent reactance estimation, (c) X/R ratio, and (d) SMC reactance superimposed by its average value.

These graphs demonstrate VS-VIS actuation to assure the X/R control objectives during the resistance and reactance variations. However, it is crucial to observe that the insertion of x_v results in an overshoot in r_e that can affect the GF-PC power delivery. On the contrary, inserting a step variation of r_v does not provoke overshoot in the system's equivalent reactance. For that reason, an updating mechanism is employed in the proposed VS-VIS to avoid undesired transients caused by sudden virtual reactance modification.

D. COMPENSATION FOR GRID IMPEDANCE VARIATION

In this experiment, the performance of the grid impedance shaping approach under grid impedance variation is evaluated. The controlled switch S_{w1} is opened to interconnect external resistors (r_{ext}) with the PCC feeder impedance ($z_s = rs_s + jx_s$), according to Fig. 1, to provoke an X/R deviation inside the UMS dead-zone. The feeder impedance is composed of $r_s = 0.4\ \Omega$ and $l_s = 3.6$ mH (see Table 1), which leads to $X/R \approx 2.827$ for the nominal frequency of 50 Hz. Figs. 11(a) presents the experimental results for the controlled active and reactive powers in their respective setpoints $P_g^* = 900$ W and $Q_g^* = 300$ Var. The VS-VIS implements a virtual impedance composed of $r_v \approx -0.13\ \Omega$ and $x_v \approx 1.569\ \Omega$ for reaching $\widehat{r}_e \approx 0.27\ \Omega$ and $\widehat{x}_e \approx 2.7\ \Omega$, leading to $X/R \approx 10$ according to Figs. 11(b)-11(d).

At $t \approx 3$ s, the switch S_{w1} interconnects r_{ext}, increasing the equivalent resistance to approximately 0.31 Ω, as shown in Fig. 11(b), which results in $X/R \approx 8.71$, corresponding to

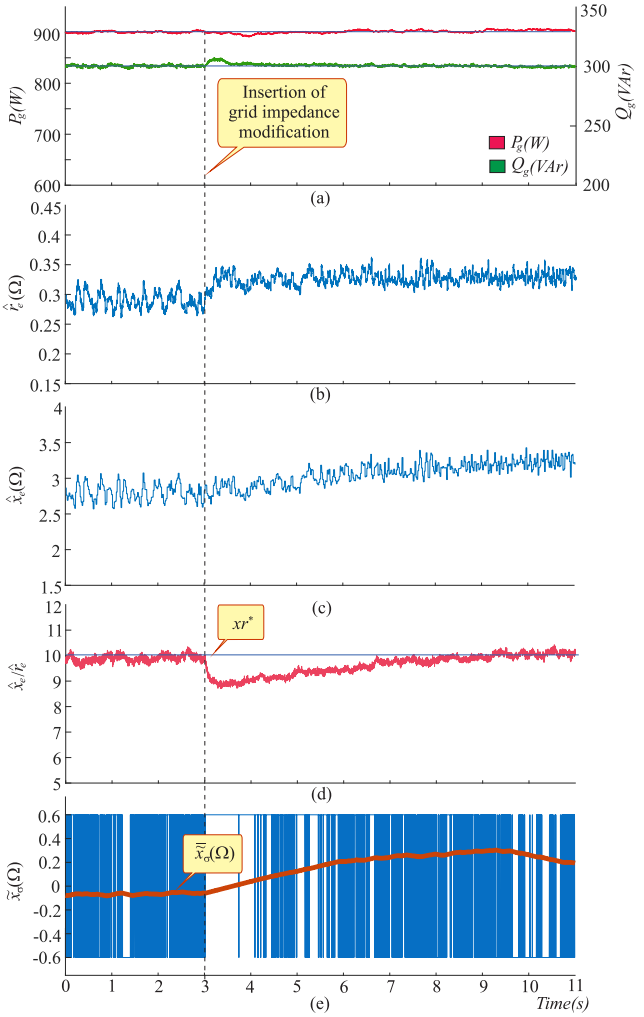

FIGURE 11. Experimental results of GF-PC under grid impedance variation; (a) delivered active and reactive powers by GF-PC, (b) equivalent resistance estimation, (c) equivalent reactance estimation, (d) X/R ratio and (e) SMC reactance superimposed by its average value.

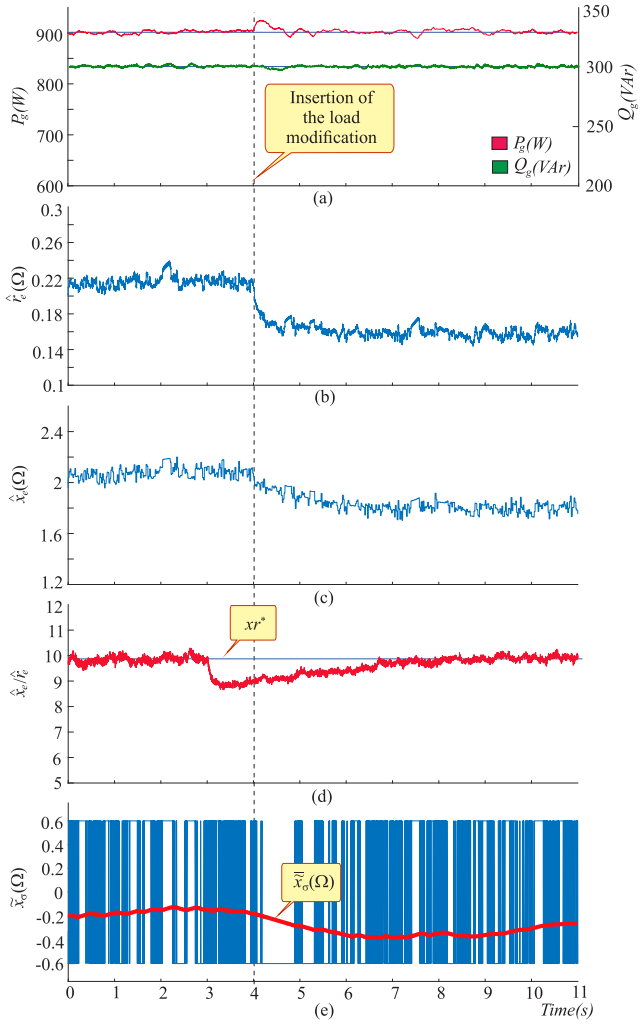

FIGURE 12. Experimental results of GF-PC under load variation; (a) delivered active and reactive powers by GF-PC, (b) equivalent resistance estimation, (c) equivalent reactance estimation, (d) X/R ratio and (e) SMC reactance superimposed by its average value.

a deviation of $|\Delta xr(t_k)| \approx 1.29$, according to Fig. 11(d). The maximum X/R deviation is fixed in $\Delta xr_{\max} \approx 1.5$, which means that the UMS will not update the virtual reactance x_v. As a result, the SMC virtual reactance approach increases the average values of $\widetilde{x}_\sigma$ (i.e., $\widetilde{x}_\sigma = \beta_0 sgn(\sigma)$, the SMC switching control law of u_{eq} in the Eq. (40) to reach the desired $X/R = 10$, as it can be verified in Figs 11(c)-11(e). These experimental results demonstrate that the proposed SMC virtual impedance can compensate for mismatches provoked by grid impedance variations inside the X/R dead zone.

E. OPERATION UNDER LOAD VARIATION

This test evaluates the performance of the grid impedance shaping scheme under load variation, which can indirectly cause grid impedance ranges, affecting power flow control schemes. An RL three-phase load ($z_l = r_l + jx_l$) is connected to the PCC in this operational scenario. The controlled switch S_{w2} interconnects a three-phase resistive load (r_{lext}) parallel with the z_l, provoking a load variation that results in an X/R ratio change inside the dead zone.

Figs. 12(a) presents the experimental results of the controlled active and reactive powers regulated in the same setpoints of the test before. With the inclusion of the load, the VS-VIS implements a virtual impedance composed of $r_v \approx -0.18\ \Omega$ and $x_v \approx 1.069\ \Omega$ for reaching $\widehat{r}_e \approx 0.22\ \Omega$ and $\widehat{x}_e \approx 2.2\ \Omega$, leading to $X/R \approx 10$ according to Figs. 12(b)-12(d).

At $t \approx 4$ s, the switch S_{w2} interconnects the r_{lext} parallel with the z_l, reducing the equivalent resistance $\widehat{r}_e = 0.16\ \Omega$, as shown in Fig. 12(b). The load variation changes the grid impedance parameters, resulting in $\widehat{x}_e/\widehat{r}_e \approx 8.82$, as depicted in Fig. 12(d), which corresponds to a deviation of $|\Delta xr(t_k)| \approx 1.18$. Like the test before, the maximum X/R deviation is fixed at 1.5, restraining x_v updating. As a result, the SMC virtual reactance $\widetilde{x}_v$ decreases its average values to achieve the X/R control objective, as observed in Figs 12(c)-12(e). The controlled active and reactive powers depict a slight transient

during the load change but quickly converge to their setpoints. These experimental results demonstrate the capabilities of the proposed grid shaping approach in dealing with load change occurrences.

V. CONCLUSION

This paper proposes an adaptive grid impedance shaping approach to enhance the power flow control of GF-PC. In this system, a decision logic system determines the required virtual impedance based on the X/R ratio provided by the grid impedance estimator, network damping condition, and GF-PC power availability. The present solution employs a virtual impedance composed of negative virtual resistance in series connected with a positive reactance. The resistive component is calculated and implemented continuously using a standard methodology, while the reactance employs a VS-VIS. In this scheme, the required virtual reactance is determined in each sampling time, but the implemented value is only updated when the X/R variations cause PCC voltage deviations that extrapolate the limits imposed by the standards. Furthermore, the virtual reactance is split into standard virtual and SMC reactances for assuring the grid shaping objectives. The first implements the main part of the required virtual reactance, and the second provides a fine-tuning control action to match the necessary virtual reactance. Also, the modeling and design concepts of the proposed method are fully detailed. Besides, the implementation algorithm employs only basic mathematical and logical operations, making it simple to be embedded into the GF-PC systems. Also, Nyquist stability studies demonstrated that the design criteria adopted to set up the voltage controller gains and define the parameters of the proposed grid-shaping approach assure the system's stability up to the physical limits of the power converter. Moreover, the proposed method provides a grid-shaping action with smooth transients, which improves the resilience of the GF-PC system. Finally, the experimental results obtained from a GF-PC laboratory setup demonstrated the effectiveness of the proposed solution with different operational conditions.

REFERENCES

[1] Y. Han, H. Li, P. Shen, E. A. A. Coelho, and J. M. Guerrero, "Review of active and reactive power sharing strategies in hierarchical controlled microgrids," *IEEE Trans. Power Electron.*, vol. 32, no. 3, pp. 2427–2451, Mar. 2017.

[2] L. Ding, Q.-L. Han, and X.-M. Zhang, "Distributed secondary control for active power sharing and frequency regulation in islanded microgrids using an event-triggered communication mechanism," *IEEE Trans. Ind. Informat.*, vol. 15, no. 7, pp. 3910–3922, Jul. 2019.

[3] W. Yao, M. Chen, J. Matas, J. M. Guerrero, and Z.-M. Qian, "Design and analysis of the droop control method for parallel inverters considering the impact of the complex impedance on the power sharing," *IEEE Trans. Ind. Electron.*, vol. 58, no. 2, pp. 576–588, Feb. 2011.

[4] J. M. Guerrero, J. C. Vasquez, J. Matas, L. G. de Vicuna, and M. Castilla, "Hierarchical control of droop-controlled AC and DC microgrids—A general approach toward standardization," *IEEE Trans. Ind. Electron.*, vol. 58, no. 1, pp. 158–172, Jan. 2011.

[5] R. Razi, H. Iman-Eini, M. Hamzeh, and S. Bacha, "A novel extended impedance-power droop for accurate active and reactive power sharing in a multi-bus microgrid with complex impedances," *IEEE Trans. Smart Grid*, vol. 11, no. 5, pp. 3795–3804, Sep. 2020.

[6] C.-T. Lee, C.-C. Chu, and P.-T. Cheng, "A new droop control method for the autonomous operation of distributed energy resource interface converters," *IEEE Trans. Power Electron.*, vol. 28, no. 4, pp. 1980–1993, Apr. 2013.

[7] J. He, Y. W. Li, and F. Blaabjerg, "An enhanced islanding microgrid reactive power, imbalance power, and harmonic power sharing scheme," *IEEE Trans. Power Electron.*, vol. 30, no. 6, pp. 3389–3401, Jun. 2015.

[8] Y. Zhu, F. Zhuo, F. Wang, B. Liu, and Y. Zhao, "A wireless load sharing strategy for islanded microgrid based on feeder current sensing," *IEEE Trans. Power Electron.*, vol. 30, no. 12, pp. 6706–6719, Dec. 2015.

[9] H. Mahmood, D. Michaelson, and J. Jiang, "Accurate reactive power sharing in an islanded microgrid using adaptive virtual impedances," *IEEE Trans. Power Electron.*, vol. 30, no. 3, pp. 1605–1617, Mar. 2015.

[10] H. Han, X. Hou, J. Yang, J. Wu, M. Su, and J. M. Guerrero, "Review of power sharing control strategies for islanding operation of AC microgrids," *IEEE Trans. Smart Grid*, vol. 7, no. 1, pp. 200–215, Jan. 2016.

[11] C. Dou, Z. Zhang, D. Yue, and M. Song, "Improved droop control based on virtual impedance and virtual power source in low-voltage microgrid," *IET Gener., Transmiss. Distrib.*, vol. 11, no. 4, pp. 1046–1054, Mar. 2017.

[12] J. Zhou and P.-T. Cheng, "A modified Q—V droop control for accurate reactive power sharing in distributed generation microgrid," *IEEE Trans. Ind. Appl.*, vol. 55, no. 4, pp. 4100–4109, Jul. 2019.

[13] Q.-C. Zhong, "Robust droop controller for accurate proportional load sharing among inverters operated in parallel," *IEEE Trans. Ind. Electron.*, vol. 60, no. 4, pp. 1281–1290, Apr. 2013.

[14] J. He, Y. W. Li, J. M. Guerrero, F. Blaabjerg, and J. C. Vasquez, "An islanding microgrid power sharing approach using enhanced virtual impedance control scheme," *IEEE Trans. Power Electron.*, vol. 28, no. 11, pp. 5272–5282, Nov. 2013.

[15] M. Kosari and S. H. Hosseinian, "Decentralized reactive power sharing and frequency restoration in islanded microgrid," *IEEE Trans. Power Syst.*, vol. 32, no. 4, pp. 2901–2912, Jul. 2017.

[16] B. Liu, Z. Liu, J. Liu, R. An, H. Zheng, and Y. Shi, "An adaptive virtual impedance control scheme based on small-AC-signal injection for unbalanced and harmonic power sharing in islanded microgrids," *IEEE Trans. Power Electron.*, vol. 34, no. 12, pp. 12333–12355, Dec. 2019.

[17] Y. W. Li and C.-N. Kao, "An accurate power control strategy for power-electronics-interfaced distributed generation units operating in a low-voltage multibus microgrid," *IEEE Trans. Power Electron.*, vol. 24, no. 12, pp. 2977–2988, Dec. 2009.

[18] T. Wu, Z. Liu, J. Liu, S. Wang, and Z. You, "A unified virtual power decoupling method for droop-controlled parallel inverters in microgrids," *IEEE Trans. Power Electron.*, vol. 31, no. 8, pp. 5587–5603, Aug. 2016.

[19] Y. Zhu, F. Zhuo, F. Wang, B. Liu, R. Gou, and Y. Zhao, "A virtual impedance optimization method for reactive power sharing in networked microgrid," *IEEE Trans. Power Electron.*, vol. 31, no. 4, pp. 2890–2904, Apr. 2016.

[20] H.-J. Yoo, T.-T. Nguyen, and H.-M. Kim, "Consensus-based distributed coordination control of hybrid AC/DC microgrids," *IEEE Trans. Sustain. Energy*, vol. 11, no. 2, pp. 629–639, Apr. 2020.

[21] H. Zhang, S. Kim, Q. Sun, and J. Zhou, "Distributed adaptive virtual impedance control for accurate reactive power sharing based on consensus control in microgrids," *IEEE Trans. Smart Grid*, vol. 8, no. 4, pp. 1749–1761, Jul. 2017.

[22] J. Zhou, S. Kim, H. Zhang, Q. Sun, and R. Han, "Consensus-based distributed control for accurate reactive, harmonic, and imbalance power sharing in microgrids," *IEEE Trans. Smart Grid*, vol. 9, no. 4, pp. 2453–2467, Jul. 2018.

[23] J. Chen, D. Yue, C. Dou, L. Chen, S. Weng, and Y. Li, "A virtual complex impedance based P—$\dot{V}$ droop method for parallel-connected inverters in low-voltage AC microgrids," *IEEE Trans. Ind. Informat.*, vol. 17, no. 3, pp. 1763–1773, Mar. 2021.

[24] D. K. Alves, R. L. D. A. Ribeiro, F. B. Costa, T. D. O. A. Rocha, and J. M. Guerrero, "Wavelet-based monitor for grid impedance estimation of three-phase networks," *IEEE Trans. Ind. Electron.*, vol. 68, no. 3, pp. 2564–2574, Mar. 2021.

[25] Y. Shtessel, C. Edwards, L. Fridman, and A. Levant, *Sliding Mode Control and Observation*. New York, NY, USA: Springer, 2014.

[26] T. V. Hoang and H.-H. Lee, "An adaptive virtual impedance control scheme to eliminate the reactive-power-sharing errors in an islanding meshed microgrid," *IEEE J. Emerg. Sel. Topics Power Electron.*, vol. 6, no. 2, pp. 966–976, Jun. 2018.

[27] T. Q. Fonseca, R. L. A. Ribeiro, T. O. A. Rocha, F. B. Costa, and J. M. Guerrero, "Voltage grid supporting by using variable structure adaptive virtual impedance for LCL-VSC DG converters," *IEEE Trans. Ind. Electron.*, vol. 67, no. 11, pp. 9326–9336, Nov. 2020.
[28] W. Zhang, A. M. Cantarellas, J. Rocabert, A. Luna, and P. Rodriguez, "Synchronous power controller with flexible droop characteristics for renewable power generation systems," *IEEE Trans. Sust. Energy*, vol. 7, no. 4, pp. 1572–1582, Oct. 2016.
[29] W. Zhang, D. Remon, and P. Rodriguez, "Frequency support characteristics of grid-interactive power converters based on the synchronous power controller," *IET Renew. Power Gener.*, vol. 11, no. 4, pp. 470–479, 2017.
[30] J. He, L. Du, B. Liang, Y. Li, and C. Wang, "A coupled virtual impedance for parallel AC/DC converter based power electronics system," *IEEE Trans. Smart Grid*, vol. 10, no. 3, pp. 3387–3400, May 2019.
[31] S. M. Ashabani and Y. A. R. I. Mohamed, "New family of microgrid control and management strategies in smart distribution grids-analysis, comparison and testing," *IEEE Trans. Power Syst.*, vol. 29, no. 5, pp. 2257–2269, Sep. 2014.
[32] X. Meng, J. Liu, and Z. Liu, "A generalized droop control for grid-supporting inverter based on comparison between traditional droop control and virtual synchronous generator control," *IEEE Trans. Power Electron.*, vol. 34, no. 6, pp. 5416–5438, Sep. 2019.
[33] *IEEE Standard for Interconnecting Distributed Resources With Electric Power Systems*, IEEE Standard 1547.2, 2008, p. 219.
[34] J. Sun, "Impedance-based stability criterion for grid-connected inverters," *IEEE Trans. Power Electron.*, vol. 26, no. 11, pp. 3075–3078, Nov. 2011.
[35] B. Wen, D. Boroyevich, R. Burgos, P. Mattavelli, and Z. Shen, "Inverse Nyquist stability criterion for grid-tied inverters," *IEEE Trans. Power Electron.*, vol. 32, no. 2, pp. 1548–1556, Feb. 2017.
[36] R. D. Middlebrook, "Input filter considerations in design and application of switching regulators," in *Proc. IEEE Ind. Appl. Soc. Annu. Meeting*, Chicago, IL, USA, Oct. 1976, pp. 366–382.

RICARDO LUCIO DE ARAUJO RIBEIRO (Senior Member, IEEE) was born in Campina Grande, Brazil, in 1961. He received the B.S., M.S., and Ph.D. degrees in electrical engineering from the Federal University of Campina Grande, Campina Grande, in 1990, 1992, and 2003, respectively. From 2001 to 2002, he was a Visiting Scholar with the Department of Electrical Engineering, Politecnico di Torino, Turin, Italy. From April 2021 to March 2022, he was a Visiting Professor with AAU Energy, Aalborg University, Aalborg, Denmark. Since March 2004, he has been a Full Professor with the Department of Electrical Engineering, Federal University of Rio Grande do Norte, Natal, Brazil, and the Director of the Research Laboratory of Industrial Electronics and Renewable Energy (LEIER/UFRN). His research interests include power electronics, renewable energy systems, power quality control, energy efficiency, AC–DC microgrids, storage systems, and power system stability. He is currently a Secretary of Joint Chapter—PES/IAS/PELS—IEEE Bahia Section R9, a Tutor of the IEEE—IAS/PELS Student Branch of the Federal University of Rio Grande do Norte, and a member of the IEEE Industrial Electronics and Power Electronics Society and SOBRAEP-Brazilian Association of Power Electronics.

ARMAN OSHNOEI (Member, IEEE) received the M.S. degree in electrical engineering from the University of Tabriz, Tabriz, Iran, in 2017, and the Ph.D. degree in electrical engineering from Shahid Beheshti University, Tehran, Iran, in 2021. From November 2021 to May 2022, he was a Visiting Ph.D. Scholar with the Department of Energy, Aalborg University, Aalborg, Denmark, where he is currently a Postdoctoral Researcher. His research interests include modeling and control of power electronic-based power systems, power system stability and control, and intelligent control.

AMJAD ANVARI-MOGHADDAM (Senior Member, IEEE) received the Ph.D. degree (Hons.) in power systems engineering from the University of Tehran, in 2015. From 2015 to 2019, he was a Postdoctoral Research Fellow with Aalborg University. He is currently an Associate Professor and the Leader of the Intelligent Energy Systems and Flexible Markets (iGRIDS) Research Group, Department of Energy (AAU Energy), Aalborg University, where he is also acting as the Vice-Leader of Power Electronic Control, Reliability and System Optimization (PESYS) and the Coordinator of the Integrated Energy Systems Laboratory (IES-Laboratory). He made a Guest Professor stay with Technische Universität München, Germany, from November 2021 to December 2021. He has coauthored more than 250 technical articles, five books, and nine book chapters in the field. His research interests include planning, control and operation management of microgrids, renewable/hybrid power systems, and integrated energy systems with appropriate market mechanisms. He was a recipient of the 2020 DUO—India Fellowship Award, the DANIDA Research Fellowship Grant from the Ministry of Foreign Affairs of Denmark, in 2018 and 2021, the IEEE-CS Outstanding Leadership Award 2018, Halifax, Nova Scotia, Canada, and the 2017 IEEE-CS Outstanding Service Award, Exeter, U.K. He serves as the Associate Editor for the IEEE TRANSACTIONS ON POWER SYSTEMS, IEEE ACCESS, IEEE SYSTEMS JOURNAL, IEEE OPEN ACCESS JOURNAL OF POWER AND ENERGY, and IEEE POWER ENGINEERING LETTERS. He is the Vice-Chair of IEEE Denmark Section and the IEEE-PES Danish Chapter and serves as a Technical Committee Member of several IEEE PES/IES/PELS and CIGRE working groups.

FREDE BLAABJERG (Fellow, IEEE) received the Ph.D. degree in electrical engineering from Aalborg University, Aalborg, Denmark, in 1995. He was with ABB-Scandia, Randers, Denmark, from 1987 to 1988. He became an Assistant Professor, in 1992, an Associate Professor, in 1996, and a Full Professor of power electronics and drives with the Department of Energy Technology, Aalborg University, in 1998, where he has been a Villum Investigator, since 2017. He is currently the Honoris Causa with University Politehnica Timisoara (UPT), Timisoara, Romania, and Tallinn Technical University (TTU), Tallinn, Estonia. He has published more than 600 journal articles in the fields of power electronics and its applications. He is the coauthor of four monographs and the editor of ten books in power electronics and its applications. His current research interests include power electronics and its applications, such as in wind turbines, photovoltaic systems, reliability, harmonics, and adjustable speed drives. He received 31 IEEE Prize Paper Awards, the IEEE PELS Distinguished Service Award, in 2009, the EPE-PEMC Council Award, in 2010, the IEEE William E. Newell Power Electronics Award, in 2014, and the Villum Kann Rasmussen Research Award, in 2014. He was a recipient of the "Global Energy" Award for significant contribution to the development of technologies that provide new opportunities in energy development, in 2019. He was the President of the IEEE Power Electronics Society, from 2019 to 2020, and the Vice-President of the Danish Academy of Technical Sciences. He was the Editor-in-Chief of the IEEE TRANSACTIONS ON POWER ELECTRONICS, from 2006 to 2012. He was a Distinguished Lecturer of the IEEE Power Electronics Society, from 2005 to 2007, and the IEEE Industry Applications Society, from 2010 to 2011 and from 2017 to 2018. He was nominated (2014–2018) by Thomson Reuters to be included in the 250 most cited researchers in engineering in the world.